Available online at www.sciencedirect.com
ScienceDirect
International Journal of Heat and Mass Transfer 50 (2007) 881–896
International Journal of HEAT and MASS TRANSFER
www.elsevier.com/locate/ijhmt

Forced convection in slightly curved microchannels

Liqiu Wang *, Fang Liu

Department of Mechanical Engineering, The University of Hong Kong, Pokfulam Road, Hong Kong

Received 5 December 2005; received in revised form 18 August 2006
Available online 24 October 2006

Abstract

To address the effects of curvature, initial conditions and disturbances, a numerical study is made on the fully-developed bifurcation structure and stability of the forced convection in curved microchannels of square cross-section and curvature ratio 5×10^{-6}. No matter how small it is, the channel curvature always generates the secondary flow in the channel cross-plane which increases the mean friction factor moderately and the Nusselt number significantly. Unknown initial conditions of convection lead to the co-existence of multiple steady fully-developed flows of various structures. Ten solution branches (either symmetric or asymmetric) are found with eight symmetry-breaking bifurcation points and thirty-one limit points. Thus a rich solution structure exists with the co-existence of various flow states over certain ranges of governing parameters. Dynamic responses of the multiple steady flows to finite random disturbances are examined by the direct transient computation. It is found that possible physically realizable fully-developed flows under the effect of unknown disturbances evolve, as the Dean number increases, from a stable steady 2-cell state at lower Dean number to a temporal periodic oscillation, another stable steady 2-cell state, a temporal intermittent oscillation, and a chaotic temporal oscillation. There exist no stable steady fully-developed flows in some ranges of governing parameters. Both the mean friction factor and the mean Nusselt number are also obtained and analyzed with their correlating relations listed.

Keywords: Microchannel forced convection; Bifurcation; Multiplicity; Stability; Numerical simulation

1. Introduction

Flow in *curved* microchannels finds its applications in various microfludics devices for changing flow direction, enhancing mixing/separation/reaction, increasing channel length within a compact area and avoiding corners [1,2]. Previous studies focused mainly on the curvature-induced dispersion and the dispersion-reduction schemes [3,4]. Studies of detailed flow characteristics in curved microchannels are very limited in this relatively new and exciting field. Ref. [5] appears the only reported experimental study of friction factor of water flows in curved mini-channels of depth 0.1 mm, width varying from 0.5 to 1 mm and curvature radius from 33 to 53 mm.

As a limiting case of flow in *curved* microchannels, flow in *straight* microchannels has emerged as an important area of research during the last decade. Critical state-of-the-art reviews of literature are available, for example, in [6–8]. Previous investigations focused primarily on single-phase flow and heat transfer in trapezoidal, circular, rectangular, and parallel plate microchannels [7]. The research focus has been mainly on the applicability of classical continuum model [6], the friction factor and the heat transfer coefficient [7,8]. Here we refer the classical continuum model as the continuum model from conservations of mass, momentum and energy, linear constitutive relations of stress-strain and heat flux-temperature gradient, no-slip and no-temperature-jump boundary conditions [6].

The classical continuum model works under two conditions: the fluid is a continuum, and the flow is not too far from thermodynamic equilibrium [6]. For gases, the Knudsen number *Kn*, defined as the ratio of the mean free path to the characteristic length of the flow, determines the

---

* Corresponding author. Tel.: +852 2859 7908; fax: +852 2858 5415.
E-mail address: lqwang@hku.hk (L. Wang).

0017-9310/$ - see front matter © 2006 Elsevier Ltd. All rights reserved.
doi:10.1016/j.ijheatmasstransfer.2006.08.016

degree of rarefaction and the applicability of classical continuum model. The classical continuum model leads to fairly accurate predictions for $Kn < 0.001$. Slip and jump effects must be taken into account for $0.001 \leqslant Kn < 0.1$. For $0.1 \leqslant Kn < 10$, the classical continuum model breaks down and alternative continuum models are needed. For $Kn \geqslant 10$, the flow must be modeled as the free-molecule flow.

The density of liquids is about 1000 times the density of gases. The spacing between molecules in liquids is approximately ten times less than the spacing in gases [8]. Liquid molecules do not have a mean free path. The lattice spacing may, however, be used as a similar measure [8]. For water, the lattice spacing is 0.3 nm. In a 1-μm gap and a 50-μm-diameter channel, the equivalent Knudsen numbers are 3×10^{-4} and 6×10^{-6}, respectively, well within the range of obeying continuum flow [8]. The effects of slip and temperature jump boundary conditions will not occur either unless the channels are smaller than approximately 3 nm [8]. Thus, liquid flow and heat transfer in microchannels of hydraulic diameters ranging from 1 μm to 1 mm should be described adequately by the classical continuum model [8].

Large differences exist in the reported friction factors ($0.5 \leqslant f/f_{\text{mac}} \leqslant 5$) and heat transfer coefficients ($0.21 \leqslant Nu/Nu_{\text{mac}} \leqslant 16$) for single-phase flow through channels of hydraulic diameters ranging from 0.96 to 2.6 mm [7]. Here f and Nu are the friction factor and the Nusselt number, respectively. Subscript mac stands for macroscale predictions. Refs. [9–11] are examples of the works reporting the friction factor lower than macroscale predictions, following predictions, and higher than predictions respectively. Refs. [9,12,13] reported, on the other hand, the Nusselt number lower than macroscale predictions, following predictions, and higher than predictions respectively. There also exists a large discrepancy in the reported critical Reynolds number Re_{c} for transition from laminar to turbulent flow in microchannels [7,8]. While Re_{c} is found to be very close to that in the macrochannels in some studies [8], a much lower Re_{c} is reported in [11] and the other works. Furthermore, experiments in [14] show no transition for Reynolds numbers up to 10 000.

Suggested reasons for the derivations of liquid flow and heat transfer characteristics in straight microchannels from those of macrochannels are surface roughness effects, entrance and three-dimensional transport effects, electric double-layer (EDL) effects, channel curvature, effects of initial conditions and disturbances [7,8]. As generally accepted [7,8], however, no conclusive explanation is available at present for these phenomena. The quantification of each of these effects is not available in the literature either.

The very large differences in the reported f/f_{mac}, Nu/Nu_{mac} and Re_{c} might be an indication of the co-existence of multiple flow and heat transfer states, a signature of effects of unknown initial conditions and disturbances and a common phenomenon of nonlinear dynamic systems. While the study of multiplicity and stability is crucial for understanding of flow and heat transfer in microchannels in general, for quantification of the effects of initial conditions and disturbances and reconciliation of the inconsistencies in the reported f/f_{mac}, Nu/Nu_{mac} and Re_{c} in particular, there appears no such study available in this relatively new and exciting field.

In an attempt to examine the effects of channel curvature, initial conditions and disturbances, the present contribution addresses the fully-developed, two-dimensional bifurcation structure and stability of the forced convection in a square microchannel with a very slight curvature. The flow geometry is illustrated in Fig. 1 with (R, Z, ϕ) as the radial (normal), spanwise and streamwise directions, respectively. A viscous fluid is driven by a streamwise pressure gradient to flow through a square microchannel with a very slight streamwise curvature and a uniform wall heat flux. All microchannels used in the experiments are not perfectly straight so that a numerical simulation of flows in slightly curved microchannels is more relevant and desirable. A perfectly straight microchannel can also be reviewed as a special case of curved microchannels when $\sigma = 0$. Here σ is the curvature ratio defined by a/R_{c}, the ratio of channel width a over the radius of curvature R_{c} (Fig. 1). As the mixed convection in straight channels and the forced convection in curved channels have similar flow bifurcation and stability features [15], the results in this paper can also shed the light on the multiplicity and stability of mixed convection in straight microchannels.

As the first part of the work, we use the classical continuum model, good for liquid flows and gas flows with $Kn < 0.001$, to model the flow and heat transfer in microchannels and focus on the effects of initial conditions and disturbances without considering the effects of EDL and surface roughness. The governing differential equations in primitive variables are solved for detailed bifurcation structure by a finite-volume/Euler–Newton continuation method with the help of the bifurcation test function, the branch switching technique and the parameterization of arc-length or local variable [16,17]. Transient calculation is made to examine in detail the response of every solution family to finite random disturbances. The Hopf bifurcation can also be detected by the transient computation. The work differs from the previous studies of macroscale curved channel flows mainly on the extension to the forced convection in very slightly curved channels and the examination of the effects of initial conditions and disturbances on the forced convection in microchannels. The readers are refereed to [18] for available bifurcation structure and stability of macroscale curved channel flows in the literature.

2. Governing equations

Consider a hydrodynamically and thermally fully developed laminar flow of viscous fluid in a slightly curved square microchannel under the thermal boundary conditions of uniform wall heat flux and peripherally uniform wall temperature at any streamwise position (Fig. 1). The

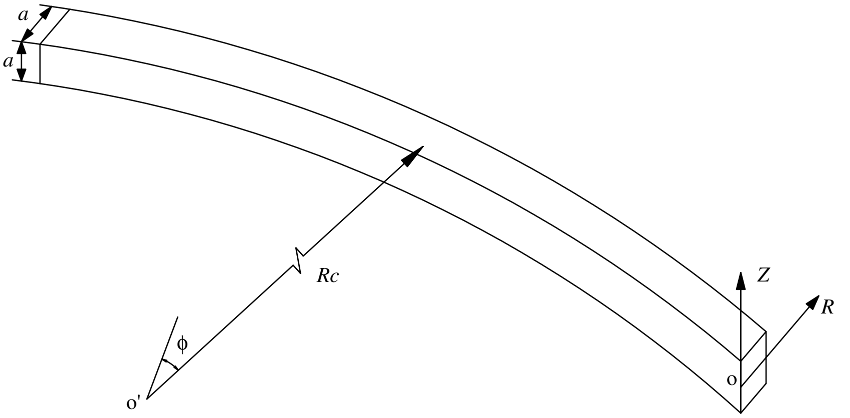

Fig. 1. Physical problem and coordinate system.

geometry is toroidal and hence the finite pitch effect is not considered. Properties of the fluid, density in particular, are taken to be constant. Therefore, a gravity potential can be introduced for the purely hydrostatic effect of gravity [15].

Consider a toroidal coordinate system (R, Z, ϕ) as shown in Fig. 1. Let U, V and W be velocity components in directions of R, Z, and ϕ respectively, t the time, and T, T_w the temperatures of the fluid and the wall. Continuity, Navier–Stokes and energy equations governing the fully developed laminar flow and heat transfer are given, in terms of dimensionless variables, as [15,18]

Continuity equation

$$\frac{\partial}{\partial r}\{[1+\sigma(r-0.5)]u\}+\frac{\partial}{\partial z}\{[1+\sigma(r-0.5)]v\}=0. \tag{1}$$

Momentum equations

$$\frac{\partial u}{\partial \tau}+u\frac{\partial u}{\partial r}+v\frac{\partial u}{\partial z}-\frac{16w^2Dk^2}{\sigma[1+\sigma(r-0.5)]} = -\frac{\partial p}{\partial r}+\left\{\frac{\partial^2 u}{\partial r^2}+\frac{\partial^2 u}{\partial z^2}+\frac{\sigma}{1+\sigma(r-0.5)}\frac{\partial u}{\partial r}-\frac{\sigma^2 u}{[1+\sigma(r-0.5)]^2}\right\}, \tag{2}$$

$$\frac{\partial v}{\partial \tau}+u\frac{\partial v}{\partial r}+v\frac{\partial v}{\partial z}=-\frac{\partial p}{\partial z}+\left[\frac{\partial^2 v}{\partial r^2}+\frac{\partial^2 v}{\partial z^2}+\frac{\sigma}{1+\sigma(r-0.5)}\frac{\partial v}{\partial r}\right], \tag{3}$$

$$\frac{\partial w}{\partial \tau}+u\frac{\partial w}{\partial r}+v\frac{\partial w}{\partial z}+\frac{\sigma uw}{1+\sigma(r-0.5)} = \frac{1}{1+\sigma(r-0.5)}+\left\{\frac{\partial^2 w}{\partial r^2}+\frac{\partial^2 w}{\partial z^2}+\frac{\sigma}{1+\sigma(r-0.5)}\frac{\partial w}{\partial r}-\frac{\sigma^2 w}{[1+\sigma(r-0.5)]^2}\right\}. \tag{4}$$

Energy equation

$$\frac{\partial \theta}{\partial \tau}+u\frac{\partial \theta}{\partial r}+v\frac{\partial \theta}{\partial z}-\frac{4wDk}{\sigma Pr[1+\sigma(r-0.5)]} = \frac{1}{Pr}\left[\frac{\partial^2 \theta}{\partial r^2}+\frac{\partial^2 \theta}{\partial z^2}+\frac{\sigma}{1+\sigma(r-0.5)}\frac{\partial \theta}{\partial r}\right]. \tag{5}$$

The dimensionless variables are defined as

$$r=\frac{R}{a},\quad z=\frac{Z}{a},\quad \tau=\frac{t}{v/a^2},\quad u=\frac{aU}{v},\quad v=\frac{aV}{v},$$

$$w=\frac{W}{W_1},\quad p=\frac{P}{\rho(v/a)^2},\quad \theta=\frac{T_w-T}{\Delta T},$$

where v and ρ are the kinematic viscosity and the density of the fluid; a is the channel radial dimension; P is a pseudo-pressure, a combination of fluid pressure and the gravity potential; W_1 and ΔT are the representative streamwise velocity and temperature difference, respectively, which are defined as

$$W_1=\frac{a^2c_1}{\mu};\quad \Delta T=Prac_2.$$

Here μ is the viscosity of the fluid; Pr, the Prandtl number; c_1, the streamwise pressure gradient which is a positive constant for hydrodynamically fully developed flow ($c_1=-\frac{\partial p'}{R_c\partial\phi}$ with R_c as the curvature radius) [15]; c_2, the streamwise temperature gradient which is a constant for the thermally fully developed flow, but can be positive or negative depending on the heating or cooling of the fluid $\left(c_2=\frac{\partial T}{R_c\partial\phi}\right)$ [15].

It is customary to use the mean streamwise velocity W_m and the difference between the wall temperature and the bulk mean temperature (T_w-T_b) for the non-dimensionalization of streamwise velocity and temperature, respectively. However, the employment of these quantities results unavoidably in the appearance of two unknown dimensional parameters in the governing equations, which comprise the unknowns W_m and T_b, respectively. Consequently, the iterative procedure should be applied, assuming some initial estimated values to them. It requires an additional computation time. In order to avoid this additional increase in computation time, we follow [15] in using W_1 and ΔT as the representative streamwise velocity and the representative temperature difference, respectively. They involve the streamwise pressure gradient c_1 and the streamwise temperature gradient c_2, which are usually given as design parameters so that it does not induce the difficulty in using computation results for design. The velocity W_1 is proportional to the pressure drop in the streamwise direction. For the flow in a stationary straight circular tube, the mean streamwise velocity W_m is related to W_1 as $W_m=W_1/8$ [15]. The temperature difference ΔT

is, on the other hand, proportional to the fluid temperature difference between the inlet and outlet of the channel.

Three dimensionless parameters are defined as, with α as the thermal diffusivity,

$$\sigma = \frac{a}{R_c}, \quad Pr = \frac{\nu}{\alpha}, \quad Dk = \frac{\sigma a W_1}{4\nu}.$$

The dimensionless groups adopted here are those in [15,18]. The curvature ratio σ is a geometry parameter, representing the degree of curvature. The Prandtl number Pr, a thermophysical property parameter, represents the ratio of momentum diffusion rate to that of thermal diffusion. Dk is a pseudo Dean number with W_1 as the characteristic velocity [15,18].

Boundary conditions (non-slip, impermeability and uniform peripheral temperature) may be written, in terms of dimensionless variables, as

$$u = v = w = \theta = 0 \quad \text{at } r = 0, 1 \quad \text{for } -0.5 \leqslant z \leqslant 0.5, \tag{6}$$

$$u = v = w = \theta = 0 \quad \text{at } z = -0.5, 0.5 \quad \text{for } 0 \leqslant r \leqslant 1. \tag{7}$$

Within the scope of the present study, the Eqs. (1)–(5) under the boundary conditions (6), and (7) constitute the mathematical model of the problem under consideration in forms of primitive variables u, v, w, p and θ. We use them to examine the steady bifurcation structure by removing all time-dependent terms. We also use them to study stability properties of multiple solutions through a direct transient computation examining dynamic responses of every steady solution family to finite random disturbances.

After the velocity and temperature fields are obtained, the computation of the local friction factor and Nusselt number is of practical interest. Following the usual definitions, the expression for the product of friction factor and Reynolds number fRe and Nusselt number Nu can be written based on the local streamwise velocity gradient and temperature gradient at the wall as [15],

$$fRe = \frac{2}{w_m}\left(\frac{\partial w}{\partial n}\right)\text{wall}, \tag{8}$$

$$Nu = \frac{1}{\theta_b}\left(\frac{\partial \theta}{\partial n}\right)\text{wall}, \tag{9}$$

where w_{m} and θ_{b} are the mean streamwise velocity and the bulk mean temperature, respectively. The mean friction factor and Nusselt number can be obtained by peripherally averaging their local values.

3. Numerical algorithm

3.1. Bifurcation structure

For steady bifurcation structure, we remove the time-dependent terms in Eqs. (2)–(5). The governing Eqs. (1)–(5) are then discretized under the boundary conditions (6) and (7) by the finite volume method which is an adaptation of that in [15,18]. Main features of this method include a staggered mesh system, a power-law formulation for the combined effect of convection and diffusion terms, and central difference scheme for source terms. After this discretization in the flow domain, we obtain a set of nonlinear algebraic equations, the so-called discretization equations, which approximate the governing differential Eqs. (1)–(5) under the boundary conditions (6) and (7) and can be written symbolically as

$$\mathbf{f}(\mathbf{y}, \boldsymbol{\alpha}) = 0, \tag{10}$$

where $\boldsymbol{\alpha} = [\sigma, Pr, Dk]$ (the parameter vector), $\mathbf{y}$ is the dependent variable vector of size N with N as the total number of equations, and $\mathbf{f}$ is a vector-valued function of size N.

Among the three parameters, the curvature ratio σ is a more detailed measure of the effect of geometry and the extent to which the centrifugal force varies on the cross section. For a very slightly curved channel, we fix its value at 5×10^{-6}. While the Prandtl number Pr affects the temperature field, it has no effect on flows because the flow field is decoupled with the temperature field for the forced convection. In the present work, we set the Pr at 7.0, a typical value for water.

Eq. (10) has a solution $\mathbf{y} = \mathbf{0}$ when $Dk = 0$. This is physically obvious and can be confirmed by a dimensional version of (1)–(7). This point serves the starting point of our continuation schemes in tracing solution branches as the control parameter λ varies. We use Dk, as the control parameter, for the regular portion of solution branches, u at $r = 0.9$ and $z = 0.14$ (Dk as one unknown variable) or the arc-length s for turning limit points [16,17]. The u at (0.9, 0.14) is selected as the control parameter λ in turning limit points because it varies significantly as Dk changes. For the case of using s as the control parameter λ in turning limit points in the arc-length continuation, we need an additional algebraic equation

$$\sum_{j=1}^{N} \left.\frac{\partial y_j}{\partial s}\right|_{s_0} [y_j(s) - y_j(s_0)] + \left.\frac{\partial Dk}{\partial s}\right|_{s_0} [Dk(s) - Dk(s_0)] - (s - s_0) = 0, \tag{11}$$

in addition to Eq. (10) which now takes the form of

$$\mathbf{f}(\mathbf{y}(s), \quad D_k(s)) = 0. \tag{12}$$

Here, $s = \|(\mathbf{y}, D_k)^T\|_2$, $s - s_0$ is the step size along the branch and y_j is a component of $\mathbf{y}$. Eq. (11) is obtained by differentiating the defining equation of s

$$\sum_{j=1}^{N} [y_j(s) - y_j(s_0)]^2 + [Dk(s) - Dk(s_0)]^2 = (s - s_0)^2$$

with respect to s.

Eq. (10) (or Eqs. (11) and (12)) is solved for the whole branch solution by Euler–Newton method for all unknown dependent variables simultaneously. Let $\mathbf{y}(\lambda_i)$ be the solution at $\lambda = \lambda_i$ which has been obtained, the Euler predictor for $\mathbf{y}(\lambda_i + \Delta\lambda)$ is, where $\Delta\lambda$ is the step size,

$$\mathbf{y}^0(\lambda_i + \Delta\lambda) = \mathbf{y}(\lambda_i) + \left.\frac{\partial \mathbf{y}}{\partial \lambda}\right|_{\lambda_i} \Delta\lambda, \tag{13}$$

where $\frac{\partial \mathbf{y}}{\partial \lambda}\big|_{\lambda_i}$ is the solution of the system of linear algebraic equations

$$\mathbf{J}|_{\mathbf{y}(\lambda_i),\lambda_i}\frac{\partial \mathbf{y}}{\partial \lambda}\bigg|_{\lambda_i} = -\frac{\partial \mathbf{f}}{\partial \lambda}\bigg|_{\lambda_i}. \tag{14}$$

Here $\mathbf{J}$ with $J_{ij} = \frac{\partial f_i}{\partial y_j}$ as components is the Jacobian matrix, and is evaluated numerically by the forward difference [17]. Linear Eq. (14) is then solved by the SPARSPAK (the Waterloo sparse matrix package), which is a collection of FORTRAN subroutines for solving large sparse systems of linear equations. The basic approach used in the SPARSPAK is to compute a triangular factorization of the coefficient matrix using Gaussian elimination without any row interchanges [17].

Using $\mathbf{y}^0(\lambda_i + \Delta\lambda)$ from the Euler-predictor (Eq. (13)) as the initial guess of $\mathbf{y}(\lambda_i + \Delta\lambda)$, the damped Newton iteration of Eq. (10) (or Eqs. (11) and (12)), in which the Jacobian matrix $\mathbf{J}$ is updated once for every four iterations, leads to:

$$\begin{aligned}&\mathbf{J}[\mathbf{y}^{k+1}(\lambda_i + \Delta\lambda) - \mathbf{y}^k(\lambda_i + \Delta\lambda)]\\&\quad = \mathbf{f}^k[\mathbf{y}^k(\lambda_i + \Delta\lambda), \lambda_i + \Delta\lambda], \quad k = 1, 2, \ldots,\end{aligned} \tag{15}$$

where k denotes the kth iteration. Eq. (15) is solved for $\mathbf{y}^{k+1}(\lambda_i + \Delta\lambda)$ by the SPARSPAK. The solution was assumed to be convergent in a numerical sense if the Euclidean norm of error in each of the primitive variables (i.e., velocity components, temperature and pressure) over all grid points is less than 10^{-10} between successive iterations.

In order to detect bifurcation points, a test function τ_{ij}, defined by [16,17]

$$\tau_{ij} = \mathbf{e}_i^T \mathbf{J}\mathbf{h} \tag{16}$$

is evaluated at every continuation step after the Newton iteration is convergent. Here, $\mathbf{e}_i$ is a unit column vector of size N and the column vector $\mathbf{h}$ of size N satisfies

$$\mathbf{J}_{ij}\mathbf{h} = \mathbf{e}_i, \tag{17}$$

where the matrix $\mathbf{J}_{ij}$ is a reduced $\mathbf{J}$ by replacing its ith row by a unit vector, i.e.,

$$\mathbf{J}_{ij} = [(\mathbf{I} - \mathbf{e}_i\mathbf{e}_i^T)\mathbf{J} + \mathbf{e}_i\mathbf{e}_j^T]. \tag{18}$$

Eq. (17) guarantees that $\mathbf{h}$ is a non-trivial solution and is solved by the SPARSPAK. When the system is at the bifurcation point (i.e., singular $\mathbf{J}$), τ_{ij} vanishes. The values of i and j can be any integer less than N. For our problem, we take the grid indexes of point $(0.9, 0.14)$ as their values. This choice works well as the flow at this point changes sensitively with Dk.

Branch switching refers to the calculation of at least one solution on the emanating branch arising at the bifurcation point. This first solution could serve as the starting point for a subsequent tracing of the entire branch. Note that at least two solutions $[\mathbf{y}(\lambda_1), \lambda_1]$ and $[\mathbf{y}(\lambda_2), \lambda_2]$ with opposite sign of the test function τ_{ij} are available close to the bifurcation in practice. We use the branch switching technique developed by Seydel [16] which approximates the difference between the branches by $\delta_0 \max\{1, |y_k(\lambda^*)|\}\mathbf{h}$.

Here, δ_0 is an empirical variable. Seydel [16] found that $\delta_0 = 0.02$ is successful for a wide range of practical problems. For our problem, a value in the range 0.01–0.04 enables us to switch branches successfully. y_k is the kth component of $\mathbf{y}$ with the index k from 1 up to N. λ^* is either λ_1 or λ_2. $\mathbf{h}$ is a column vector of size N defined and determined by Eq. (17) with $\mathbf{J}_{ij}$ evaluated at λ^* and $\mathbf{y}(\lambda^*)$. Using

$$\mathbf{y}^0(\lambda^*) = \mathbf{y}(\lambda^*) \pm \delta_0 \max\{1, |y_k(\lambda^*)|\}\mathbf{h} \tag{19}$$

as the initial guess, the damped Newton iteration of Eq. (10) (or Eqs. (11) and (12))

$$\begin{aligned}&\mathbf{J}|_{\mathbf{y}^k(\lambda*),\lambda}[\mathbf{y}^{k+1}(\lambda^*) - \mathbf{y}^k(\lambda^*)] = \mathbf{f}^k[\mathbf{y}^k(\lambda^*), \lambda^*],\\&\quad k = 1, 2, \ldots,\end{aligned} \tag{20}$$

could lead to a *first solution* on the emanating branch.

3.2. Dynamic responses to finite random disturbances

For transient computation aiming for the response of multiple steady solutions to the finite two-dimensional random disturbances, we obtain the discretization equations by integrating the governing equations with the time-dependent terms over every control volume *and* over the time period from τ to $\tau + \Delta\tau$ (the finite volume method). The fully implicit method is used because of its superior numerical stability. The system of discretization equations is then solved by the Euler-Damped Newton method described above by viewing time τ as the continuation parameter. The initial condition at $\tau = 0$, which also serves the starting point of the continuation scheme, is formed by the steady solution $\mathbf{y}_s(Dk)$ plus a finite random disturbance. Here, the subscript s denotes the steady solution. The random disturbance is generated by $d^{(k)}\chi^{(k)}\mathbf{y}_s(Dk)$. Here d is the maximum percentage of disturbing value over the steady value $\mathbf{y}_s$. The superscript k represents the ordinal of the disturbance. χ is a vector of size N whose components take random values from -1 to 1 and are generated by the computer. To examine dynamic responses of a steady solution to different finite random disturbances, we normally generate three sets of disturbances denoted by $k = 1$, 2, and 3, with $d = 5\%$, 10%, and 15% respectively.

3.3. Grid-dependence check

With the recognition that at a point in the parameter space, several different solutions with quite different flow structures can coexist, a uniform grid that is fine enough to resolve all the different flow structures appears proper. In the present computations, the grid dependence was checked by three pairs of grid sizes uniformly distributed in the flow domain. They are 50×50, 100×100 and 200×200. The pair of numbers $(L \times K)$ represents the number of grid points used in r and z-directions, respectively. The bifurcation diagrams obtained by using these three grid sizes are shown in Fig. 2 with the u velocity

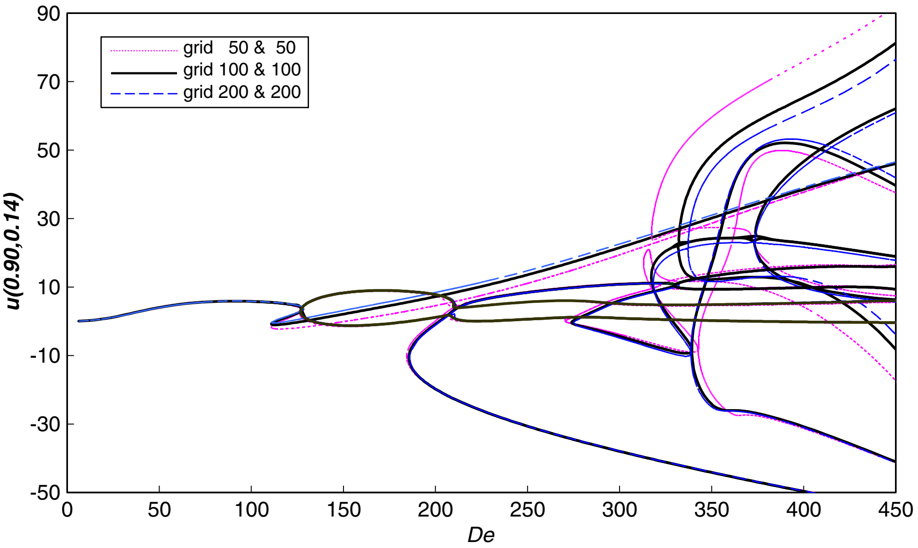

Fig. 2. Effect of grid sizes on bifurcation structure ($\sigma = 5 \times 10^{-6}$ and $Pr = 7.0$).

component at (0.9, 0.14) as the state variable and *De* as the parameter at $\sigma = 5 \times 10^{-6}$ and $Pr = 7.0$. Here *De* is the Dean number defined by $De = Re\sqrt{\sigma}$ (*Re* is the Reynolds number). Fig. 2 shows that the bifurcation diagram has no structural change for all three pairs of grid sizes. The quantitative change is also very small for most of interested region of *De* from 100 × 100 to 200 × 200. Table 1 lists location variations of some limit and bifurcation points in terms of their *De* values. The general trend of these results as the grid size is decreased tends to indicate that the solutions for the case of (100 × 100) grids are accurate to within 1% tolerance. We also checked the detailed variations of flow and temperature fields on various solution branches for different grid sizes, and found that 100 × 100 is indeed a reasonably accurate choice for the grid size. It is worth noting that the CPU time increases rapidly as the grid spacing decreases. In order to have a balance between the cost of the computer time and the accuracy of the solution, we carried out all the computations with a 100 × 100 uniform mesh for square channels.

3.4. Accuracy check

To verify the code, five representative properties obtained by the present work are shown in Table 2 together with those in [15] at $Dk = 100$, $\sigma = 0.02$ and $Pr = 0.7$, where there is only one solution. They are Reynolds number *Re* ($Re = W_m a/\nu$ with W_m as the streamwise mean

Table 1
Location variation of some limit and bifurcation points in terms of their *De* values as grid sizes

Points	Grids	*De*	Points	Grids	*De*	Points	Grids	*De*
S_1^1	50 × 50	127.42	S_2^1	50 × 50	184.35	A_4^1	50 × 50	317.31
	100 × 100	128.09		100 × 100	185.66		100 × 100	331.78
	200 × 200	128.26		200 × 200	186.02		200 × 200	337.11
S_1^2	50 × 50	110.80	S_2^2	50 × 50	321.39	$A_5^1(B_5)$	50 × 50	/
	100 × 100	110.90		100 × 100	330.24		100 × 100	370.56
	200 × 200	110.93		200 × 200	332.49		200 × 200	373.23
A_1^1	50 × 50	126.28	S_2^3	50 × 50	270.49	B_1	50 × 50	126.46
	100 × 100	126.74		100 × 100	273.93		100 × 100	126.85
	200 × 200	126.95		200 × 200	275.02		200 × 200	127.03
A_1^2	50 × 50	/	S_2^4	50 × 50	342.62	B_2	50 × 50	321.39
	100 × 100	209.80		100 × 100	339.25		100 × 100	329.82
	200 × 200	210.60		200 × 200	338.85		200 × 200	332.49
A_1^3	50 × 50	/	S_2^5	50 × 50	312.99	B_4	50 × 50	/
	100 × 100	209.66		100 × 100	317.24		100 × 100	332.42
	200 × 200	210.34		200 × 200	318.35		200 × 200	337.11
A_1^4	50 × 50	/	A_2^1	50 × 50	321.39			
	100 × 100	209.80		100 × 100	329.76			
	200 × 200	210.61		200 × 200	332.49			
A_1^5	50 × 50	/	$A_3^1(B_3)$	50 × 50	342.62			
	100 × 100	209.66		100 × 100	339.23			
	200 × 200	210.34		200 × 200	338.74			

Table 2
Comparison of five representative properties at $Dk = 100$, $\sigma = 0.02$, $Pr = 0.7$ with those in [15]

Sources	Re	De	$\|\psi\|_{\max}$	$w_{\max}$	$\theta_{\max}$
Present work	541	76.5	5.528	0.0494	39.7
[15]	542	76.6	5.641	0.0496	39.9

Table 3
Locations of S_1^1, S_1^2, S_2^1 and B_1: a comparison with those in [19]

	S_1^1	S_1^2	S_2^1	B_1
Present work	129.55	112.82	187.91	128.22
[19]	131.13	113.35	190.77	129.71

velocity), Dean number ($De = \mathrm{Re}\sqrt{\sigma}$), maximum of absolute values of secondary flow stream function ($|\psi|_{\max}$), maximum streamwise velocity ($w_{\max}$) and maximum temperature ($\theta_{\max}$). The results are in good agreement, with a very small difference (less than 2%) being due to the different numerical methods used in the two studies. We also compared, in Table 3, the locations (in terms of their De values) of three limit points S_1^1, S_1^2, S_2^1 and one bifurcation point B_1 with those available in [19] at $\sigma = 0.02$ (see next section for the notation of limit points). The results of the present analysis are also in good agreement with those in [19]. The very small difference (less than 1.5%) is believed to be due to the different numerical methods used in the two studies. The code was also used in our previous works [18,20,21], showing that it works very well with good convergency and high accuracy.

4. Results and discussion

4.1. Solution structure

The bifurcation structure is shown in Fig. 3 for De values from 0 up to 2250 at $\sigma = 5 \times 10^{-6}$ and $Pr = 7.0$. In Fig. 3, the u velocity at (0.9, 0.14) is used as the state variable, enabling the most clear visualization of all solution branches. Ten solution branches, labeled by S_1, S_2 and A_1–A_8 respectively, are found. Here, S stands for symmetric solutions with respect to the horizontal central plane $z = 0$ and A for asymmetric solutions. Branch A_1 is bifurcated from S_1 at the symmetry-breaking bifurcation point B_1. Branches A_2–A_8 are bifurcated from S_2 at seven symmetry-breaking bifurcation points B_2–B_8, respectively. Two symmetric branches S_1, S_2 are isolated with each other. Table 4 lists De values of eight symmetry-breaking bifurcation points B_1–B_8 and thirty-one limit points labeled by their branch symbol with a superscript number. For example, S_1^2 represents the second limit point on the solution branch S_1. To visualize the details of branch connectivity and some limit points, the locally enlarged state diagrams are also shown in Fig. 3. As Fig. 3 is only 1 D projection of N dimensional solution branches, all intersecting points except eight bifurcation points should not be interpreted as connection points of branches.

Therefore, unknown initial conditions lead to the coexistence of multiple steady fully-developed flows when $De > 110.90$ (S_1^2). Each of these multiple flows corresponds to different initial conditions of flow.

The primary branch S_1 is a symmetric solution branch (Fig. 3(b)). It has two limit points S_1^1 and S_1^2. The two limit points divide the branch into three parts S_{1-1}, S_{1-2} and S_{1-3}, and generate a range ($110.90 < De < 128.09$) where three steady solutions co-exist for a fixed value of De. The secondary flows for these three sub-branches are the 2-cell state (one pair of Ekman vortices, Fig. 4(a)), the weak 4-cell state with one pair of Ekman vortices and one pair of weak Dean vortices, and the 4-cell state with one pair of Ekman vortices and one pair of Dean vortices (Fig. 4(b)), respectively. In the figure, the stream function is normalized by its maximum absolute values $|\psi|_{\max}$. A vortex with a positive (negative) value of the secondary flow stream function indicates a counter-clockwise (clockwise) circulation. The Ekman vortices are the signature of pressure gradients induced by the upper and lower walls [15,18]. The Dean vortices come from a centrifugal instability (also called Dean instability in the literature) [15,18]. The readers are referred to [15] for a detailed discussion of 2-cell and 4-cell flow structures in general, their relations with physical mechanisms and driving forces and their effects on the flow resistance and heat transfer in particular.

In addition to the two limit points S_1^1 and S_1^2, the primary branch S_1 also has a symmetry-breaking bifurcation point B_1 at $De = 126.85$ (Fig. 3(b)), originating an asymmetric solution branch A_1 (Fig. 3(c)). A_1 has five limit points A_1^1–A_1^5. The limit point A_1^1 divides the branch into upper sub-branch A_{1-1} and lower sub-branch A_{1-2}. The flows on A_{1-2} can be formed by mirror images of corresponding flows on A_{1-1} at the same De. While the sub-branch A_{1-1} contributes, through the two limit points A_1^2 and A_1^3, three flow states for any value of De in a very small range $209.66 < De < 209.80$, the difference among these three flow states is negligibly small. The flow on A_{1-1} is essentially an asymmetric 2-cell state as shown in Fig. 4(c).

The solution branch S_2 is an isolated symmetric branch (Fig. 3(d)). It is divided into seven sub-branches S_{2-1}–S_{2-7} by seven limit points S_2^1–S_2^7. The flow on S_{2-1} is a 4-cell state (Fig. 4(d)). However, this 4-cell structure differs from the one on S_{1-3} (Fig. 4(b)) mainly on the shape and size of Dean vortices. Two Dean vortices here stretch along span direction rather than the radial direction. The spanwise distance between centers of two Dean vortices is noticeably larger than that of the 4-cell flow on S_{1-3}. The flow on S_{2-2} is a 2-cell state, which is qualitatively similar to that on S_{1-1} (Fig. 4(a)), but with a stronger secondary flow. The flow on S_{2-3} is a weak 4-cell state with a pair of very weak Dean vortices.

The limit point S_2^3 leads the weakly 4-cell flow on S_{2-3} to a 6-cell state on S_{2-4} with two pairs of Dean vortices along the outer wall (Fig. 4(e)). The second pair appears because

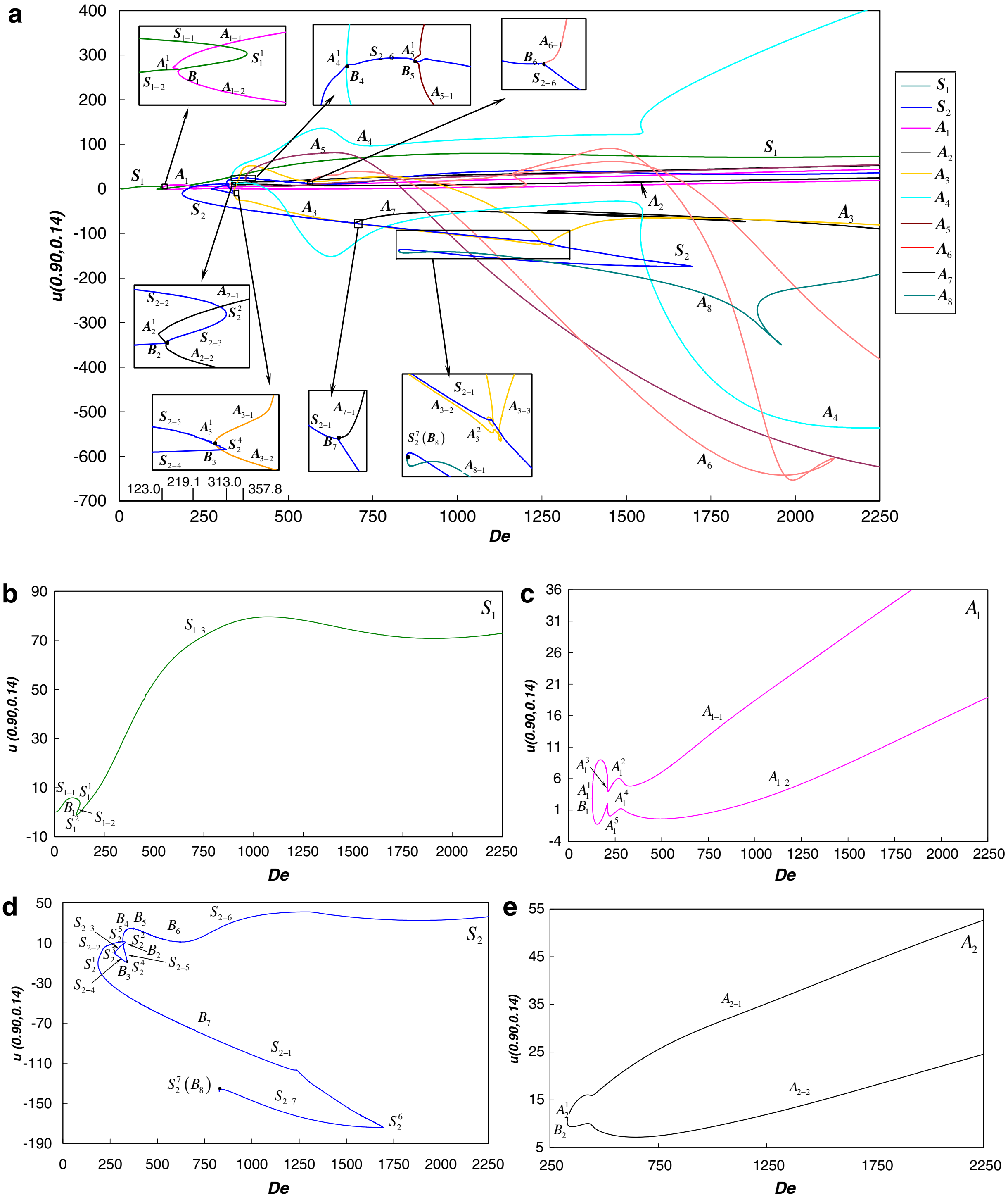

Fig. 3. Solution branches and their connectivity ($\sigma = 5 \times 10^{-6}$ and $Pr = 7.0$).

of the splitting of the original pair. It could be interesting to study, in the future, the relation between this vortex splitting and the one due to the Eckhaus instability [22]. The secondary flow on this sub-branch evolves to a stronger one through the growth of second pair of Dean vortices as *De* increases. The flows on S_{2-5} and S_{2-6} are, at low *De*, an 8-cell state with three pairs of Dean vortices (Fig. 4(f)). The third pair is formed from the outer wall. This differs from the mechanism responsible for the appearance of the second pair. As usual, the secondary flows on S_{2-5} and S_{2-6} becomes stronger as *De* increases. For the same value of *De*, the 8-cell structure on S_{2-6}, the third pair of Dean vortices in particular, is stronger than that on S_{2-5}. As *De* increases, the three pairs of Dean vortices merge together and the flow on S_{2-6} becomes a 4-cell state (Fig. 4(g)). The flow on S_{2-7} is a 6-cell state with

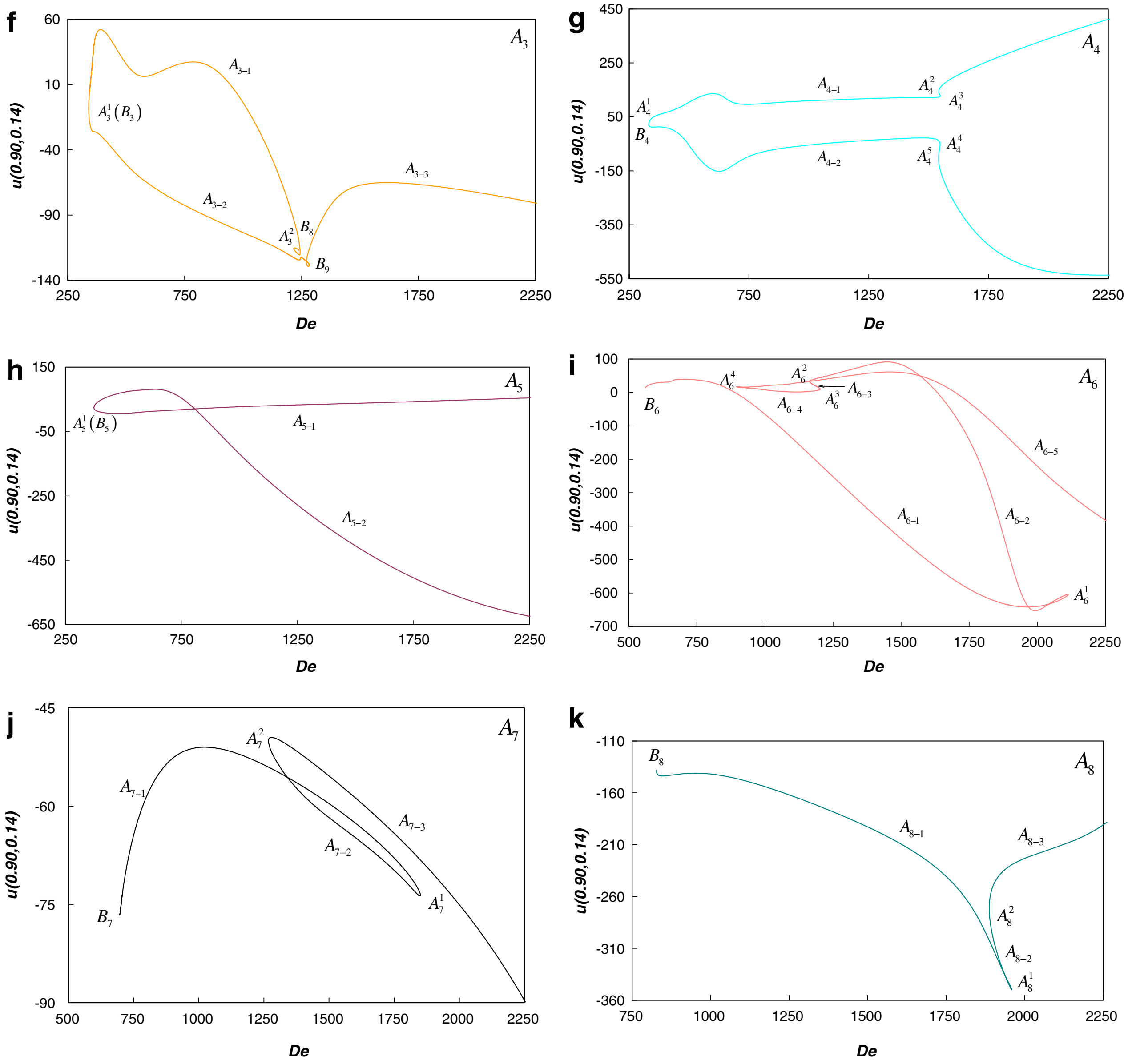

Fig. 3 (*continued*)

Table 4
Locations of all limit points and bifurcation points up to $De = 2250$ at $\sigma = 5 \times 10^{-6}$ and $Pr = 7.0$

Points	De	Points	De	Points	De	Points	De
S_1^1	128.09	S_2^4	339.25	A_4^4	1547.83	A_8^2	1887.14
S_1^2	110.90	S_2^5	317.24	A_4^5	1541.65	B_1	126.85
A_1^1	126.74	S_2^6	1693.80	$A_5^1(B_5)$	370.56	B_2	329.82
A_1^2	209.80	S_2^7	826.76	A_6^1	2113.64	B_4	332.42
A_1^3	209.66	A_2^1	329.76	A_6^2	1163.73	B_6	556.63
A_1^4	209.80	$A_3^1(B_3)$	339.24	A_6^3	1202.57	B_7	694.94
A_1^5	209.66	A_3^2	1243.92	A_6^4	895.087	B_8	826.76
S_2^1	185.66	A_4^1	331.78	A_7^1	1850.78		
S_2^2	330.24	A_4^2	1542.52	A_7^2	1267.33		
S_2^3	273.93	A_4^3	1548.77	A_8^1	1958.75		

one pair of Ekman vortices and two pairs of Dean vortices (Fig. 4(h)).

In addition to the seven limit points, the solution branch S_2 has also seven symmetry-breaking bifurcation points

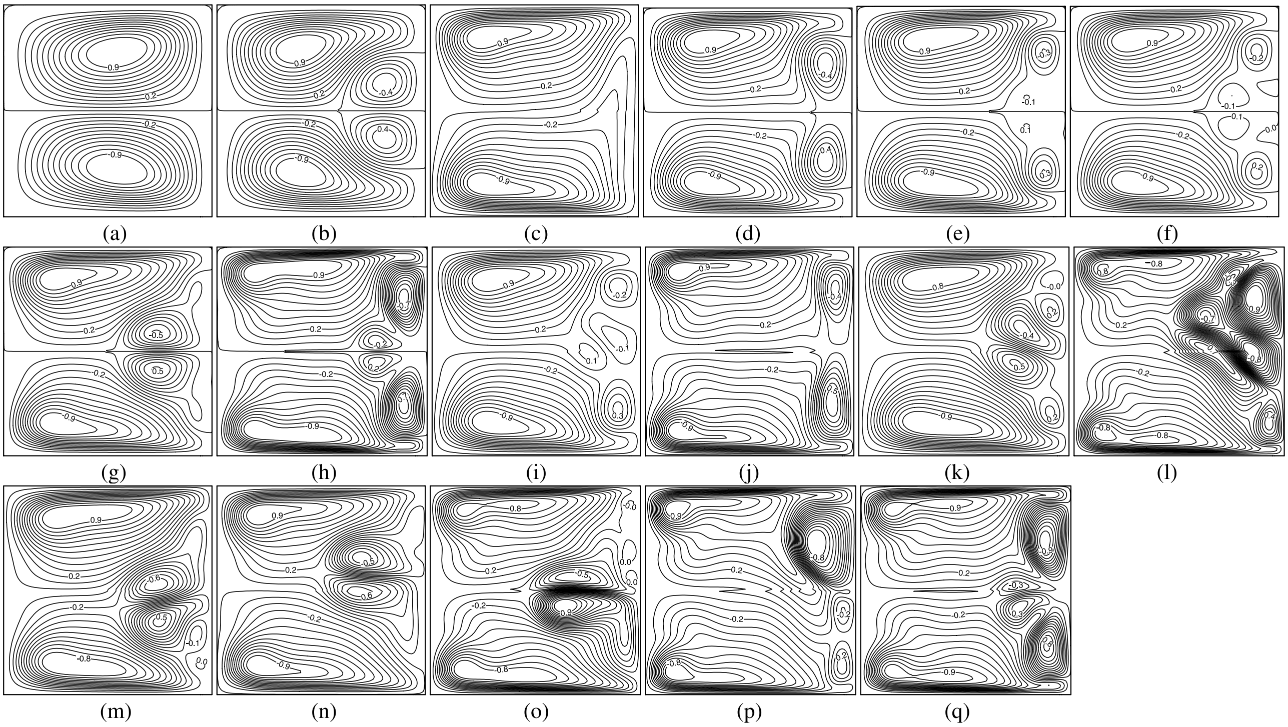
(a) (b) (c) (d) (e) (f) (g) (h) (i) (j) (k) (l) (m) (n) (o) (p) (q)

Fig. 4. Typical secondary flows on various solution sub-branches. (a) $De = 89.4$ on S_{1-1}; (b) $De = 118.5$ on S_{1-3}; (c) $De = 447.2$ on A_{1-1}; (d) $De = 335.4$ on S_{2-1}; (e) $De = 315.8$ on S_{2-4}; (f) $De = 335.4$ on S_{2-5}; (g) $De = 447.2$ on S_{2-6}; (h) $De = 894.4$ on S_{2-7}; (i) $De = 357.8$ on A_{3-1}; (j) $De = 1341.6$ on A_{3-1}; (k) $De = 357.8$ on A_{4-1}; (l) $De = 1788.9$ on A_{4-1}; (m) $De = 447.2$ on A_{5-1}; (n) $De = 670.8$ on A_{6-1}; (o) $De = 1185.1$ on A_{6-3}; (p) $De = 1565.2$ on A_{7-3} and (q) $De = 1341.6$ on A_{8-1}.

B_2–B_8 (Fig. 3(d)), originating seven asymmetric solution branches A_2–A_8, respectively. Branch A_2 has one limit point A_2^1 dividing the branch into an upper sub-branch A_{2-1} and a lower sub-branch A_{2-2} (Fig. 3(e)). Flows on the lower sub-branches are the mirror images of the corresponding flows on the upper sub-branches at the same De. The flow on A_{2-1} is an asymmetric 2-cell state (qualitatively similar to that on A_{1-1}, Fig. 4(c)). Branch A_3 has two limit points A_3^1 and A_3^2 (Fig. 3(f)). The two limit points divide the branch into three parts A_{3-1}, A_{3-2} and A_{3-3}. The secondary flow on A_{3-1} is a 5-cell state at low De values (Fig. 4(i)), but a 4-cell state at high De values (Fig. 4(j)). Flows on A_{3-2} are also asymmetric and 5-cell, mirror images of corresponding flows on A_{3-1} at the same De. The flow on A_{3-3} is, on the other hand, a 4-cell state (qualitatively similar to that in Fig. 4(j)).

Branch A_4 has five limit points A_4^1–A_4^5 (Fig. 3(g)). The limit point A_4^1 divides the branch into upper sub-branch A_{4-1} and lower sub-branch A_{4-2}. Flows on A_{4-2} can be formed by mirror images of corresponding flows on A_{4-1} at the same De. While the sub-branch A_{4-1} contributes, through the two limit points A_4^2 and A_4^3, three flow states for any value of De in a very small range $1542.52 < De < 1548.77$, the difference among these three flow states is negligibly small. The flow on A_{4-1} is essentially an asymmetric 7-cell state as shown in Fig. 4(k) and (l).

The limit point A_5^1 divides the branch A_5 into two sub-branches A_{5-1} and A_{5-2} (Fig. 3(h)). Flows on the latter are the mirror images of the former at the same De. The flow on A_{5-1} is asymmetric and 5-cell (Fig. 4(m)). Branch A_6 has five sub-branches A_{6-1}–A_{6-5} divides by the four limit points A_6^1–A_6^4 (Fig. 3(i)). Flows on these sub-branches are shown in Fig. 4(n)–(o). Branch A_7 has two limit points A_7^1 and A_7^2 (Fig. 3(j)). Flows are 4-cell on both sub-branches A_{7-1} and A_{7-2} (qualitatively similar to that in Fig. 4(j)), but 5-cell on sub-branch A_{7-3} (Fig. 4(p)). Branch A_8 has also two limit points (A_8^1 and A_8^2; Fig. 3(k)). Flows are 6-cell on all three sub-branches A_{8-1}–A_{8-3} (Fig. 4(q)).

It is interesting to note that there always exist secondary flows in the cross-plane of curved microchannels even with a very slight curvature over whole range of Dean number. The flows in the curved microchannels are thus at least two-dimensional.

4.2. Stability of multiple steady flows

Recognizing that there is no study of dynamic responses of multiple flows to finite random disturbances in the literature, a relatively comprehensive transient computation is made to examine the dynamic behavior and stability of typical steady flows with respect to three sets of finite random disturbances with $d = 5\%$, 10%, and 15% respectively. It is found that the final dynamic evolution after a short transient temporal period is independent of the initial disturbances for all steady flows in the region $0 \leqslant De \leqslant 357.77$. The results presented in this paper are those obtained from the disturbance with $d = 10\%$ unless otherwise stated. At any fixed value of De in the range $0 \leqslant De \leqslant 313.05$, all steady solutions develop, after initial finite random disturbances, to the same final state. There is no co-existence of two or more stable states in this range within the scope of the present study. The flow stability on the sub-branch S_{2-2} changes as De changes even without passing any bifurcation or limit point. In particular, the sub-branch is unstable in the range $185.66 \leqslant De \leqslant 219.13$, stable in the range $219.13 < De \leqslant 313.05$, and unstable again in the range $313.05 < De \leqslant 330.24$.

Five sub-ranges are identified with each having distinct dynamic responses to the finite random disturbances. The first is from $De = 0$ to $De = 128.09$ (S_1^1), where the finite random disturbances lead all steady flows at any fixed De to a 2-cell steady state on $S_{1-1}$with the same De. The second covers the range $128.09 < De \leqslant 219.13$where all steady flows evolve to a temporally periodic flow. In the third sub-range $219.13 < De \leqslant 313.05$, the finite random disturbances lead all steady flows to a 2-cell steady state on S_{2-2} with the same De. The fourth sub-range ranges from $De = 313.05$ to $De = 357.77$ where the steady flows response to the finite random disturbances in the form of temporal oscillation with intermittency, a forecasting signal of chaotic flows. In the last sub-range $De > 357.77$, any finite random disturbance will deviate steady flows to a chaotic oscillation.

4.3. $0 \leqslant De \leqslant 128.09$

Fig. 5(a) typifies the responses of flows on S_{1-1} to finite random disturbances. In the figure, the deviation of velocity components from their initial steady values is plotted against the time τ at (0.9, 0.14), (0.94, 0.1) and (0.96, 0.06) for $De = 89.44$. We plot both radial (u-) and spanwise (v-) velocity components for the first point (0.9, 0.14) while only u-velocity component is shown for the last two points. To facilitate the comparison, we use these four velocity components (either velocity itself or derivation velocity from its initial steady value) in all figures illustrating dynamic responses of multiple steady flows to the finite random disturbances. It is observed that all deviation velocities vanish after a short period of time. The flows and temperature profiles return to their initial steady ones shown in Fig. 4(a). Therefore, the flow on S_{1-1} is stable with respect to the finite random disturbances.

Fig. 5(b) illustrates the typical response of flows on S_{1-3} to finite random disturbances. It shows that the finite random disturbances lead eventually the flows on this unstable sub-branch to the stable one on S_{1-1} at the same De. This is further be confirmed by our detailed check of flow and temperature fields and is also true for the flows on S_{1-2}. Therefore, the steady flows on S_{1-2} and S_{1-3} are unstable to finite random disturbances and response the disturbances by evolving to the stable solution on S_{1-1} at the same De.

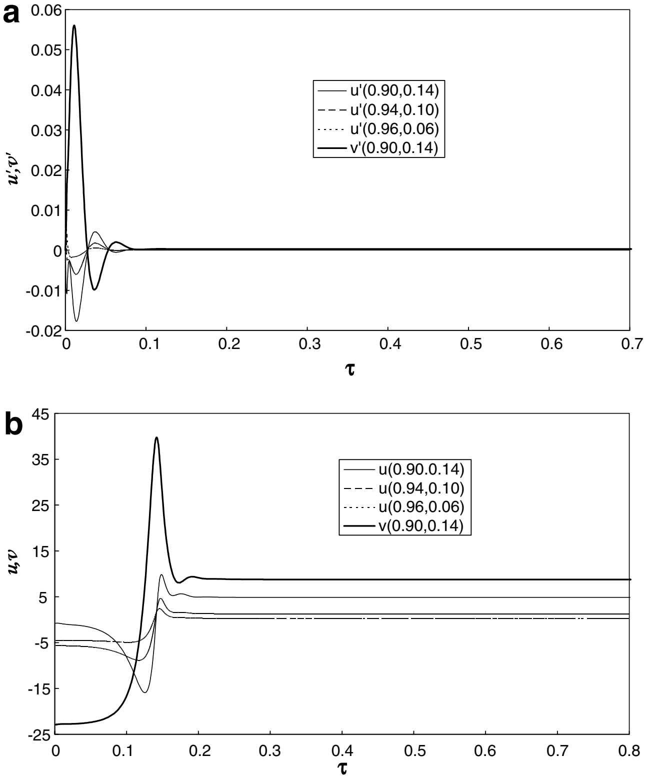

Fig. 5. Dynamic response of two solutions to finite random disturbances: evolution to stable steady 2-cell state on S_{1-1}. (a) $De = 89.44$ on S_{1-1}. (b) $De = 118.51$ on S_{1-3}.

4.4. $128.09 < De \leqslant 219.13$

The dynamic response of the solution at $De = 214.66$ on S_{2-2} is shown in Fig. 6(a). The finite random disturbances here lead the flow to a temporal periodic oscillation with a period of 0.113. Some typical secondary flow patters are detailed in Fig. 6(b) within one period of dimensionless time τ. We clearly observe the temporal oscillations between symmetric/asymmetric 2-cell flows and symmetric/asymmetric 4-cell flows. A detailed study by the dynamic responses of steady flows on the other branches at $De = 214.66$ and the comparison of flow and temperature fields within one period show that the finite random disturbances lead all the flows at the same De to the same periodic oscillation.

A similar dynamic evolution pattern exists for all cases with different values of De. This signals the similarity of flow and temperature fields within one period among the periodic oscillations at different values of De in the range $128.09 < De \leqslant 219.13$. Our detailed examination of flow and temperature fields has confirmed this, and shown that the flow structures in Fig. 6(b) are typical for all De in this range.

The dynamic responses of steady flows on A_1 in this range tend to show that B_1 is a subcritical Hopf bifurcation point.

4.5. $219.13 < De \leqslant 313.05$

The 2-cell flow on S_{2-2} is stable to the finite random disturbances in this sub-range. This can be referred by the

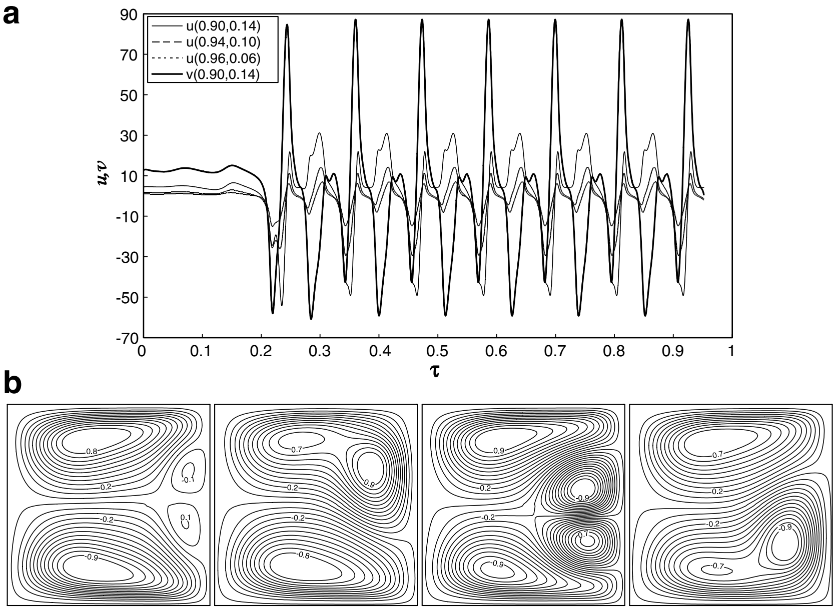

τ= 0.7850 0.8130 0.8500 0.8705

Fig. 6. Response to finite random disturbances in form of periodic oscillation in $128.09 < De \leqslant 219.13$. (a) Dynamic response of the solution at $De = 214.66$ on S_{2-2} to finite random disturbances: periodic oscillation (period = 0.113). (b) Typical secondary flow patterns in one period of temporal periodic oscillation from the solution at $De = 214.66$ on S_{2-2}.

typical response of the flow at $De = 223.61$ on this sub-branch to disturbances in Fig. 7(a). Another striking feature can be obtained by comparing the dynamic process in Fig. 7(a) with that in Fig. 5. The transient flows approach their stable steady states asymptotically for S_{1-1}, but in oscillation for S_{2-2}. The oscillation in Fig. 7(a) may be reviewed as the over-damped oscillation with the damping effect being weaker at higher *De*, and thus a longer oscillating time.

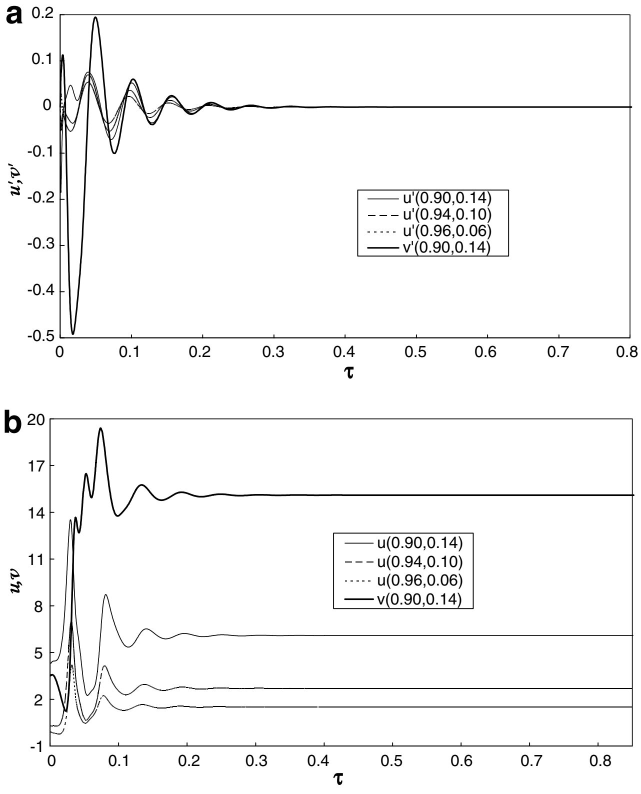

Fig. 7. Dynamic responses of solutions to finite random disturbances: evolution to stable steady 2-cell state on S_{2-2}. (a) $De = 223.61$ on S_{2-2}. (b) $De = 223.61$ on A_{1-1}.

In this sub-range of the parameter space, the finite random disturbances will lead all the other steady flows to the 2-cell steady state on S_{2-2} at the same *De*. Fig. 7(b) typifies this process by the dynamic response of the steady flow at $De = 223.61$ on A_{1-1} to disturbances.

4.6. $313.05 < De \leqslant 357.77$

In this sub-range, all solution branches are unstable. S_{2-2}, in particular, loses its stability gained in the last sub-range. While three sets of finite random disturbances lead each flow to the same final temporal oscillation, the flows at different solution branches at the same *De* respond the disturbances differently in the sense that the final oscillation is different. However, for a fixed value of *De*, all the oscillation are around the steady flows on S_{2-2} before $De = 330.24$ (point S_2^2) and around the steady flows on A_2 after $De = 330.24$. Whether A_{2-1} or A_{2-2} is difficult to distinguish because they are very close. Therefore, S_{2-2} and A_2 differ from the other solution branches in this aspect.

Fig. 8 details dynamic response to the disturbances of the steady flows at $De = 324.23$ on S_{1-3} (Fig. 8(a)). It is observed that there exist intermittent aperiodic bursts in the oscillation, one of routes to chaos [16]. The oscillation is quasi-periodic between two bursts with the periodicity

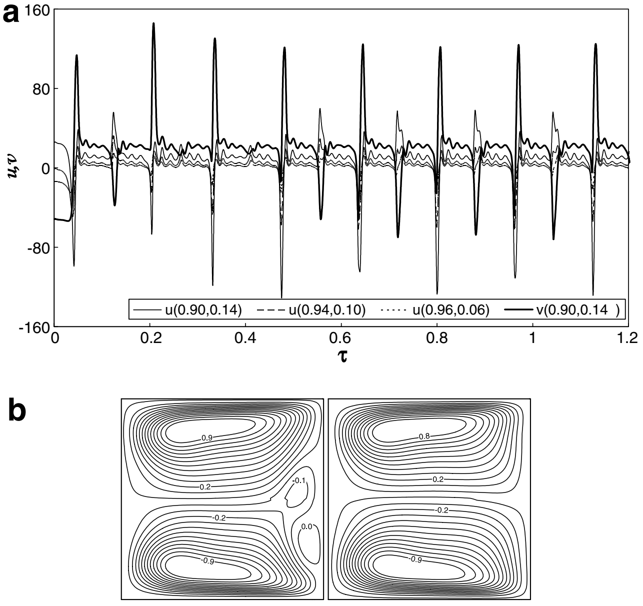

(i) τ = 0.8665 (ii) 0.9640

Fig. 8. Response to finite random disturbances in form of intermittent oscillation in $313.05 < De < 357.77$. (a) Dynamic response of the solution at $De = 324.23$ on S_{1-3} to finite random disturbances. (b) Typical secondary flow patterns of intermittent flow from solution at $De = 324.23$ on S_{1-3}.

being degraded and the appearance frequency of bursts being increased as *De* increases.

Fig. 8(b) details the secondary flow during quasi-periodic oscillations (ii) and bursts (i) for the case shown in Fig. 8(a). It is observed that the flow oscillates among symmetric/asymmetric 2-cell patterns during quasi-periodic oscillations, but among symmetric/asymmetric 4-cell structures during bursts.

4.7. *De* > 357.77

Fig. 9(a) shows the dynamic response of the flow at $De = 447.21$ on S_{1-3} to finite random disturbance with $d = 10\%$. The bursts are still observed, but with a high appearance frequency and a generally small amplitude. The oscillation between two bursts, however, cannot be reviewed as quasi-periodic any more. The Hilbert spectra of four temporal velocity series in Fig. 9(a) are constructed by the Hilbert transformation and shown in Fig. 9(b) [23]. They contain a broad-band noise, indicating the flow being chaotic [16] (This has also been confirmed by the sensitivity to the initial conditions). As *De* increases, the chaotic feature of oscillating flows becomes stronger. Fig. 9(c) details some typical secondary flow patterns during the temporally chaotic flow shown in Fig. 9(a). It is observed that the flow oscillates among 4-cell patterns during bursts (ii in Fig. 9(c)), but among 2-cell structures during the other period (i in Fig. 9(c)).

The transition from the intermittent oscillation to the chaotic oscillation is believed to be a smooth process characterized by the increase of appearance frequency and the decrease of the amplitude of bursts as the increase of *De*.

4.8. Friction factor and Nusselt number

For engineering applications, the most important results are friction factor and Nusselt number. Since the friction

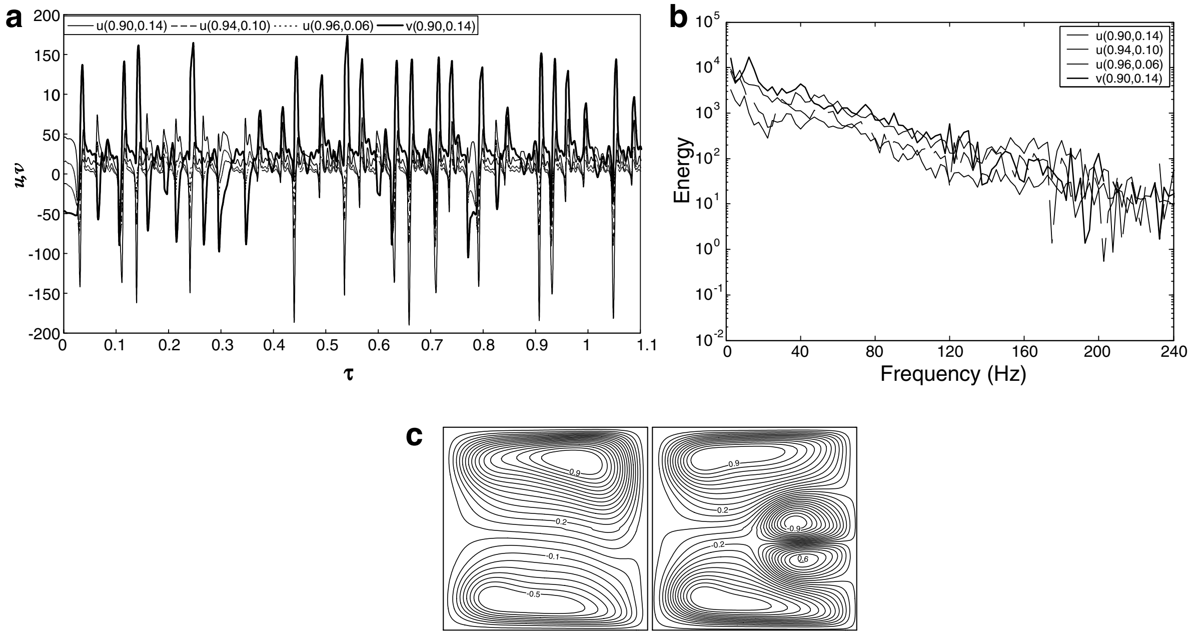

(i) τ = 0.7180 (ii) 0.7530

Fig. 9. Dynamic response to finite random disturbances: chaotic oscillation. (a) $De = 447.21$ on S_{1-3}. (b) Hilbert spectrum of the chaotic oscillation in (a). (c) Typical secondary flow patterns of chaotic flow on S_{1-3} at $De = 447.21$.

factor and Nusselt number depend on flow and temperature fields, the multiplicity and stability will strongly affect both their distributions and their mean values.

Variations of the spatial mean friction factor and the spatial mean Nusselt number as the Dean number are shown in Fig. 10(a). They are shown for the physically-

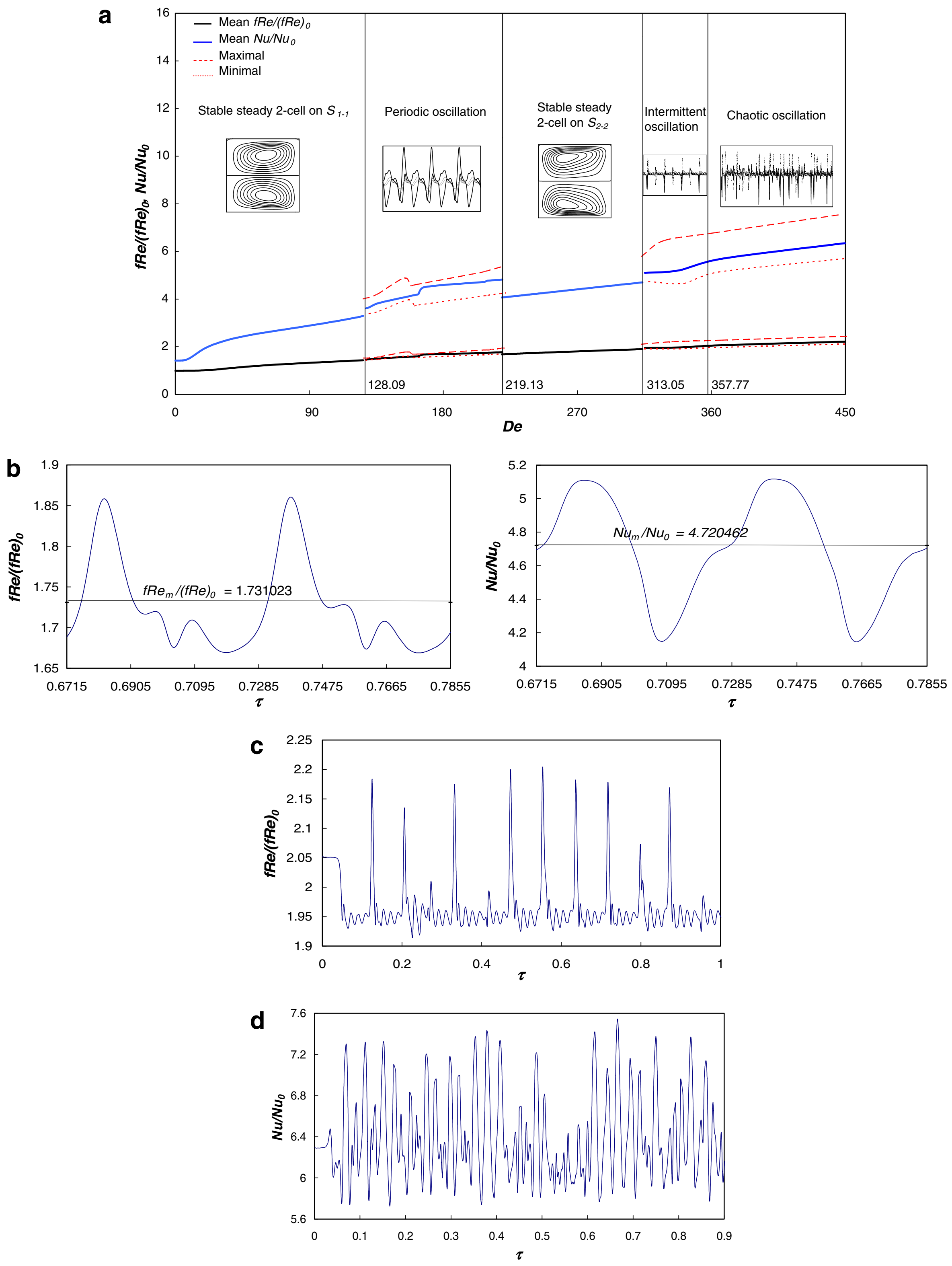

Fig. 10. Mean friction factor and mean Nusselt number. (a) Variations of the mean friction factor and the mean Nusselt number as the Dean number De. (b) Periodic oscillation of the mean friction factor and the mean Nusselt number: $De = 214.66$ on S_{2-1}. (c) Intermittent oscillation of the mean friction factor: $De = 324.23$ on S_{1-3}. (d) Chaotic oscillation of the mean Nusselt number: $De = 447.21$ on S_{1-3}.

Table 5
Correlating relations of mean friction factors and mean Nusselt numbers

Range	$fRe/(fRe)_0$	Nu/Nu_0
$0 < De \leqslant 450$	$0.96194+0.01035De^{0.78715}$	
$0 < De \leqslant 128.09$		$1.30118+0.05617De^{0.74442}$
$128.09 < De \leqslant 219.13$		$0.32187De^{0.50376}$
$219.13 < De \leqslant 313.05$		$0.067De^{2.5867}$
$313.05 < De \leqslant 450$		$0.13099De^{0.6357}$

realizable fully-developed flows under the effects of both initial conditions and disturbances and on the basis of their values for a straight duct [$(fRe)_0 = 14.23$; $Nu_0 = 3.608$] to illustrate the curvature effect. For the periodic flows in $128.09 < De \leqslant 219.13$, the mean friction and the mean Nusselt number in Fig. 10(a) are those averaged over a period. They are also averaged over an enough long period of time for either the intermittent or the chaotic flows in $De > 313.05$. For the oscillating flows in $128.09 < De \leqslant 219.13$ or in $De > 313.05$, both minimal and maximal values of the mean friction factor and the mean Nusselt number are also shown in Fig. 10(a) with their typical temporal oscillations shown in Fig. 10(b)–(d). Table 5 lists the correlating relations of mean friction factors and mean Nusselt numbers which fit quiet well with the data in Fig. 10(a).

Therefore, both the mean friction factor and the mean Nusselt number of convection in curved microchannels even with a very slight curvature are higher than their counterparts in perfectly straight channels (Fig. 10(a)). This comes apparently from the secondary flow and becomes more appreciable as De increases. The reported high experimental values of f/f_{mac} and Nu/Nu_{mac} may thus partly be from the effect of channel curvature.

Associated with the shift between stable steady flows and temporal oscillating flows, a drastic change in the mean Nusselt number is observed (Fig. 10(a)). However, this significant change does not appear for the mean friction factor which increases quite smoothly as De increases over the whole range. There appears no transition from laminar to turbulent flow for Dean numbers up to 450. Another very interesting feature is that the Nusselt number ratio is much higher than the friction factor ratio for all De values, and the difference becomes more remarkable as De increases. We can therefore significantly enhance the heat transfer by the secondary flow in curved microchannels at the expense of very slight increase of resistance to the flow.

There exist no stable steady fully-developed flows in the range $128.09 < De \leqslant 219.13$ and in the range $De > 313.05$ so that both the mean friction factor and the mean Nusselt number are at temporal oscillation in these ranges. It appears necessary to re-examine the prevalent assumption in the literature of existence of stable steady fully-developed flows in all ranges. A temporal oscillation in the friction factor and the Nusselt number could, in turn, generate the oscillation of pumping system and thermal stress in practice, which can cause the failure of pumping system and equipments.

5. Concluding remarks

In an attempt to quantify the effects of channel curvature, initial conditions and disturbances, a numerical study is made on the fully-developed bifurcation structure and stability of the forced convection in curved microchannels of square cross-section and curvature ratio 5×10^{-6}. The governing differential equations from the conservation laws are discretized by the finite volume method to obtain discretization equations, a set of nonlinear algebraic equations. The discretization equations are solved for parameter-dependence of flow and temperature fields by the Euler–Newton continuation with the solution branches parameterized by the pseudo Dean number, the arclength or the local variable. The bifurcation points are detected by the test function. The Hopf bifurcation point is determined by the transient computation. The branch switching is made by a scheme approximating the difference between branches. Two symmetric and eight asymmetric solution branches are found with eight symmetry-breaking bifurcation points and thirty-one limit points.

The dynamic responses of multiple steady flows to the 2D finite random disturbances are examined by the direct transient computation. The flows are found to respond to three sets of finite random disturbances in the same manner in the range $0 \leqslant De \leqslant 357.77$. At any fixed value of Dean number in the range $0 \leqslant De \leqslant 313.05$, all steady flows develop, after the initial finite random disturbances, to the same final state. The finite random disturbances lead the multiple steady flows to a stable steady 2-cell state on S_{1-1} in $0 \leqslant De \leqslant 128.09$, a temporal periodic oscillation between symmetric/asymmetric 2-cell flows and symmetric/asymmetric 4-cell flows in $128.09 < De \leqslant 219.13$, another stable steady 2-cell state on S_{2-2} in $219.13 < De \leqslant 313.05$, a temporal oscillation with the intermittency around the steady solution on S_{2-2} before the limit point S_2^2 and on A_2 after S_2^2 in $313.05 < De \leqslant 355.77$, and a chaotic oscillation around the steady solution on A_2 in $De > 357.77$. The intermittent flow is characterized by the flow oscillation among the symmetric/asymmetric 2-cell patterns during the period between two bursts and among the symmetric/asymmetric 4-cell structures during the burst. The chaotic flow is, on the other hand, featured by the flow oscillation among the 4-cell patterns during the burst, and the 2-cell structures during the other period.

Both the mean friction factor and the mean Nusselt number are obtained with their correlating relations listed in Table 5 for all physically-realizable fully-developed flows. The channel curvature can enhance the heat transfer significantly at the expense of slight increase of flow resistance. The drastic change of mean Nusselt number occurs when flows shift between the stable steady flows and the temporal oscillating flows.

The channel curvature, the flow multiplicity and the stability are at least partially responsible for the large differences in the reported friction factors and heat transfer coefficients in the literature, and should be further studied in order to provide the tools necessary for optimal design and process control of various MEMS and modern instruments used in chemical analysis and biomedical diagnostics (currently, the microchannel flows in biomedical diagnostics are limited to those with a low value of Dean number). New functional microdevices can also be produced by creatively using or tailoring multiple states of flows and heat transfer in microchannels.

Acknowledgements

Authors are indebted to Dr. T.L. Yang for his discussion on numerical methods and computer code. The financial support from the Research Grants Council of Hong Kong (RGC:HKU7049/06P) to LW is gratefully acknowledged.

References

[1] C.T. Culbertson, S.C. Jacobson, J.M. Ramsey, Microchip devices for high-efficiency separations, Anal. Chem. 72 (2000) 5814–5881.

[2] Y. Yamaguchi, F. Takagi, T. Watari, K. Yamashita, H. Nakamura, H. Shimizu, H. Maeda, Interface configuration of the two layered laminar flow in a curved microchannel, Chem. Eng. J. 101 (2004) 367–372.

[3] S.K. Griffiths, R.H. Nilson, Low-dispersion turns and junctions for microchannel systems, Anal. Chem. 73 (2001) 272–278.

[4] C.H. Tsai, C.H. Tai, L.M. Fu, F.B. Wu, Experimental and numerical analysis of the geometry effects of low-dispersion turns in microfluidic systems, J. Micromech. Microeng. 15 (2005) 377–385.

[5] W.H. Yang, J.Z. Zhang, H.E. Cheng, The study of flow characteristics of curved microchannel, Appl. Thermal Eng. 25 (2005) 1894–1907.

[6] M. Gad-el-Hak, in: M. Gad-el-Hak (Ed.), Flow physics, 4, CRC MEMS Handbook, 2002, pp. 1–38.

[7] S.S. Mehendale, A.M. Jacobi, R.K. Shah, Flow and heat transfer at micro- and meso-scales with application to heat exchanger design, Appl. Mech. Rev. 53 (2000) 175–193.

[8] K.V. Sharp, R.J. Adrian, J.G. Santiago, J.I. Molho, in: M. Gad-el-Hak (Ed.), Liquid flow in microchannels, 6, CRC MEMS Handbook, 2002, pp. 1–38.

[9] T.M. Harms, M.J. Kazmieczak, F.M. Gerner, Developing convective heat transfer in deep rectangular microchannels, Int. J. Heat Fluid Flow 20 (1999) 149–157.

[10] J. Judy, D. Maynes, B.W. Webb, Characterization of frictional pressure drop for liquid flows through microchannels, Int. J. Heat Mass Transfer 45 (2002) 3477–3489.

[11] G.M. Mala, D.Q. Li, Flow character of water in microtubes, Int. J. Heat Fluid Flow 20 (1999) 142–148.

[12] T.M. Adams, M.F. Dowling, S.I. Abdel-Khalik, S.M. Jeter, Applicability of traditional turbulent single-phase forced convection correlations to non-circular microchannels, Int. J. Heat Mass Transfer 42 (1999) 4411–4415.

[13] T.M. Adams, S.I. Abdel-Khalik, S.M. Jeter, Z.H. Qureshi, An experimental investigation of single-phase forced convection in microchannels, Int. J. Heat Mass Transfer 41 (1998) 851–857.

[14] R.S. Stanley, Two-Phase Flow in Microchannels, PhD Thesis, Louisiana Technological University, 1997.

[15] L.Q. Wang, K.C. Cheng, Flow transitions and combined free and forced convective heat transfer in rotating curved channels: the case of positive rotation, Phys. Fluids 8 (1996) 1553–1573.

[16] R. Seydel, Practical Bifurcation and Stability Analysis: From Equilibrium to Chaos, Springer-Verlag, New York, 1994.

[17] L.Q. Wang, H.C. Wei, X.S. Zhou, Engineering Numerical Analysis, Shandong University Press, Jinan, 2002.

[18] L.Q. Wang, T.L. Yang, Multiplicity and stability of convection in curved ducts: review and progress, Adv. Heat Transfer 38 (2004) 203–256.

[19] K.H. Winters, A bifurcation study of laminar flow in a curved tube of rectangular cross-section, J. Fluid Mech. 180 (1987) 342–369.

[20] T.L. Yang, L.Q. Wang, Bifurcation and stability of combined free and forced convection in rotating curved ducts of square cross-section, Int. J. Heat Mass Transfer 46 (2003) 613–629.

[21] L.Q. Wang, T.L. Yang, Bifurcation and stability of forced convection in curved ducts of square cross-section, Int. J. Heat Mass Transfer 47 (2004) 2971–2987.

[22] Y. Guo, W.H. Finlay, Splitting, merging and wavelength selection of vortices in curved and/or rotating channel flow due to Eckhaus instability, J. Fluid Mech. 228 (1991) 661–691.

[23] N.E. Huang, Z. Shen, S.R. Long, M.C. Wu, H.H. Shin, Q. Zheng, N.C. Yen, C.C. Tung, H.H. Liu, The empirical mode decomposition and the Hilbert spectrum for nonlinear and non-stationary time series analysis, Pro. R Soc. Lond. A 454 (1998) 903–995.